Computerized Medical Imaging and Graphics 41 (2015) 80–92

Contents lists available at ScienceDirect

Computerized Medical Imaging and Graphics

journal homepage: www.elsevier.com/locate/compmedimag

Atlas-based liver segmentation and hepatic fat-fraction assessment for clinical trials

Zhennan Yan[a], Shaoting Zhang[b,*], Chaowei Tan[a], Hongxing Qin[c], Boubakeur Belaroussi[d], Hui Jing Yu[d], Colin Miller[d], Dimitris N. Metaxas[a]

[a] CBIM, Rutgers University, Piscataway, NJ, USA
[b] Department of Computer Science, UNC Charlotte, Charlotte, NC, USA
[c] Chongqing University of Posts & Telecommunications, Chongqing, China
[d] BioClinica Inc., Newtown, PA, USA

ARTICLE INFO

Article history:
Received 11 January 2014
Received in revised form 30 March 2014
Accepted 29 May 2014

Keywords:
Hepatic fat-fraction assessment
Segmentation
Deformable model
Statistical atlas

ABSTRACT

Automated assessment of hepatic fat-fraction is clinically important. A robust and precise segmentation would enable accurate, objective and consistent measurement of hepatic fat-fraction for disease quantification, therapy monitoring and drug development. However, segmenting the liver in clinical trials is a challenging task due to the variability of liver anatomy as well as the diverse sources the images were acquired from. In this paper, we propose an automated and robust framework for liver segmentation and assessment. It uses single statistical atlas registration to initialize a robust deformable model to obtain fine segmentation. Fat-fraction map is computed by using chemical shift based method in the delineated region of liver. This proposed method is validated on 14 abdominal magnetic resonance (MR) volumetric scans. The qualitative and quantitative comparisons show that our proposed method can achieve better segmentation accuracy with less variance comparing with two other atlas-based methods. Experimental results demonstrate the promises of our assessment framework.

1. Introduction

Fatty liver, also known as hepatic steatosis, is a worldwide common condition characterized by fat accumulation in liver cells. If more than 5–10% of the liver's total weight is fat, it is called a fatty liver. It is associated with many fatty liver diseases (FLD), like alcoholic liver disease, non-alcoholic fatty liver disease (NAFLD) and steatohepatitis [1,2]. NAFLD may affect people of any age and progress to end-stage liver diseases [3]. The prevalence of NAFLD may be as high as 30% in the United States [4] and 10–24% of general population in various countries [3]. Therefore, the clinical diagnosis of fatty liver disease is very important. The diagnosis procedure often requires imaging studies, such as ultrasonography [5], X-ray computed tomography (CT) [6], magnetic resonance imaging (MRI) [7,8] and magnetic resonance spectroscopy (MRS) [9]. It has been shown that MRI and MRS are better choices for accurate detection and quantification of the hepatic fat than ultrasonography and CT [9]. Particularly, MRS is regarded as the most direct MR-based method to quantify water and fat components in liver. However, it is not widely applicable across standard clinical imaging centers due to the technical complexity. Instead, MRI based hepatic fat-fraction measurement is widely used. It employs multi-echo chemical shift based methods and computes the fat-fraction image based on the separation of fat and water (sample images in Fig. 1). So far, most studies focus on improving the quantification of fat and water components, while the estimated fat-fraction images are not liver specific. Doctors or clinical experts need to manually delineate regions of interest (ROI) and interpret the results in the whole MR images. Thus, segmentation is necessary for quantitative assessment of the fat-fraction in the liver region particularly. A clinical trial is a medical research study which is conducted for the purpose of clinical research or drug development from a large number of samples. Since 3D manual delineation of whole liver is low-efficient, high-cost and inconsistent, an automated and robust 3D liver segmentation is essential for large-dataset analysis in clinical trials.

However, there are some challenges in liver segmentation. First, nearby organs may have similar intensity levels as liver tissue which may cause misleading boundaries. Second, there exist unknown noises and imaging artifacts in medical images, which can impact the accuracy of image analysis. Bias field is a low-frequency noise which can cause intensity inhomogeneities in MR

* Corresponding author. Tel.: +1 7329919820.
E-mail address: rutgers.shaoting@gmail.com (S. Zhang).

http://dx.doi.org/10.1016/j.compmedimag.2014.05.012
0895-6111/

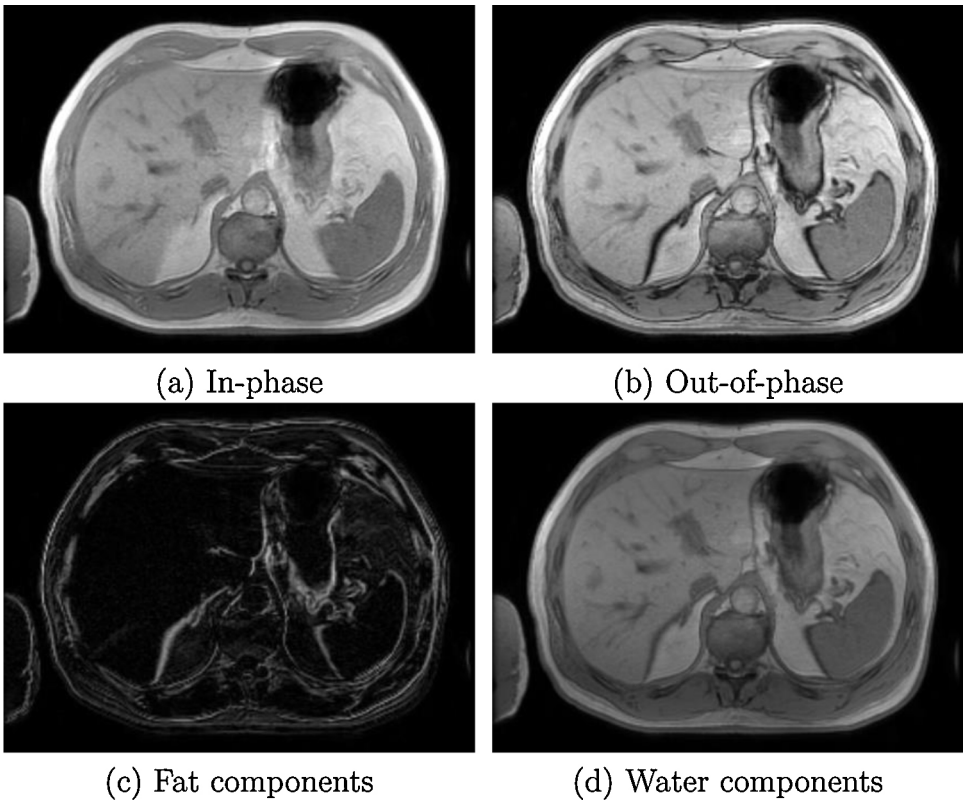

Fig. 1. Dual-phase MRI and fat/water separation.

images and lead to ambiguous object boundaries. Such ambiguous boundary cues may mislead traditional segmentation methods like region growing and edge detection to include adjacent organs. Third, liver shapes have large variance. Its morphology and structure may change due to liver affecting disorders and diseases. Besides, the collected data in clinical trials is usually from various imaging centers, using different imaging equipment's, different imaging protocols and scanning parameters. Fig. 2 shows several MR images in a FLD clinical trial. They have different sizes, spacing's and intensity patterns although they are all T1 weighted MR images. Thus, obtaining robust liver segmentation in MRI is especially challenging for datasets in clinical trials.

In recent decades, many approaches have been proposed to segment human organs or tissues in different modalities [10]. Some are interactive methods, such as graph cut algorithm [11] based segmentations [12]. Some are automatic techniques, including model based methods [13–18], learning based methods [19–23], atlas-guided approaches [24–30], and so on. Usually, learning based approaches require large amount of consistent training data which could be label intensive in practice. Owing to the variety of data in clinical trials and limited amount of training samples, most learning based segmentations are hardly applied. Deformable model based methods [31,32] are accurate but sensitive to initialization. Atlas-guided approaches rely on image registration algorithms [33–36] and most apply voxel classification to get fine segmentations [37,38]. Usually, an atlas is defined as a pair of an intensity image and its corresponding annotation (mask or label image). Due to the registration errors, atlas-guided methods are most used in segmenting objects with similar pathological and geometric characteristics (e.g. normal-appearance brains).

Here we propose an automated and robust framework for liver segmentation. It only needs a small number of training data without constraining imaging settings. Therefore, it is ideal for the hepatic fat-fraction assessment in clinical trials. In our framework, a statistical image atlas is constructed and employed to obtain a rough estimation of liver ROI. Then, a robust deformable model with shape prior is initialized from this estimation. Energy terms from edge and region information as well as the initial ROI are combined in this model for accurate and robust segmentation. The proposed segmentation method combines the reliability of atlas-based approach with the accuracy of deformable models. It is automatic and robust to various liver shapes, and different image qualities. With the segmentation result, we are able to measure the liver-specific fat-fraction distribution by magnitude-based chemical shift method [7]. We evaluate this method on a dataset of 14 volumetric MRI's from a FLD clinical trial.

The rest of the paper is organized as follows. Section 2 reviews relevant work of liver segmentations in different modalities, and the popular deformable models, shape priors and atlas construction methods. Section 3 presents the framework of our atlas-based deformable model and its application in the hepatic fat assessment. Section 4 shows the experimental results on a dataset from FLD clinical trial and discussions. Finally, Section 5 gives concluding remarks and discusses future work.

2. Related work

Many studies have shown different liver segmentation methods in recent years. Most of these segment liver in CT images [39]. Gao et al. [40] developed an automatic liver segmentation system by combining domain specific histogram analysis, morphologic operations and the deformable contour model. Beichel et al. [12] utilized an interactive segmentation method based on graph cut. Liu et al. [41] proposed a semi-automatic method using gradient vector flow (GVF) model [15] for liver segmentation in contrast-enhanced CT. Ling et al. [19] proposed a hierarchical shape representation and learning based boundary localization technique. Kainmüller et al. [42] used a statistical shape constrained free form deformable

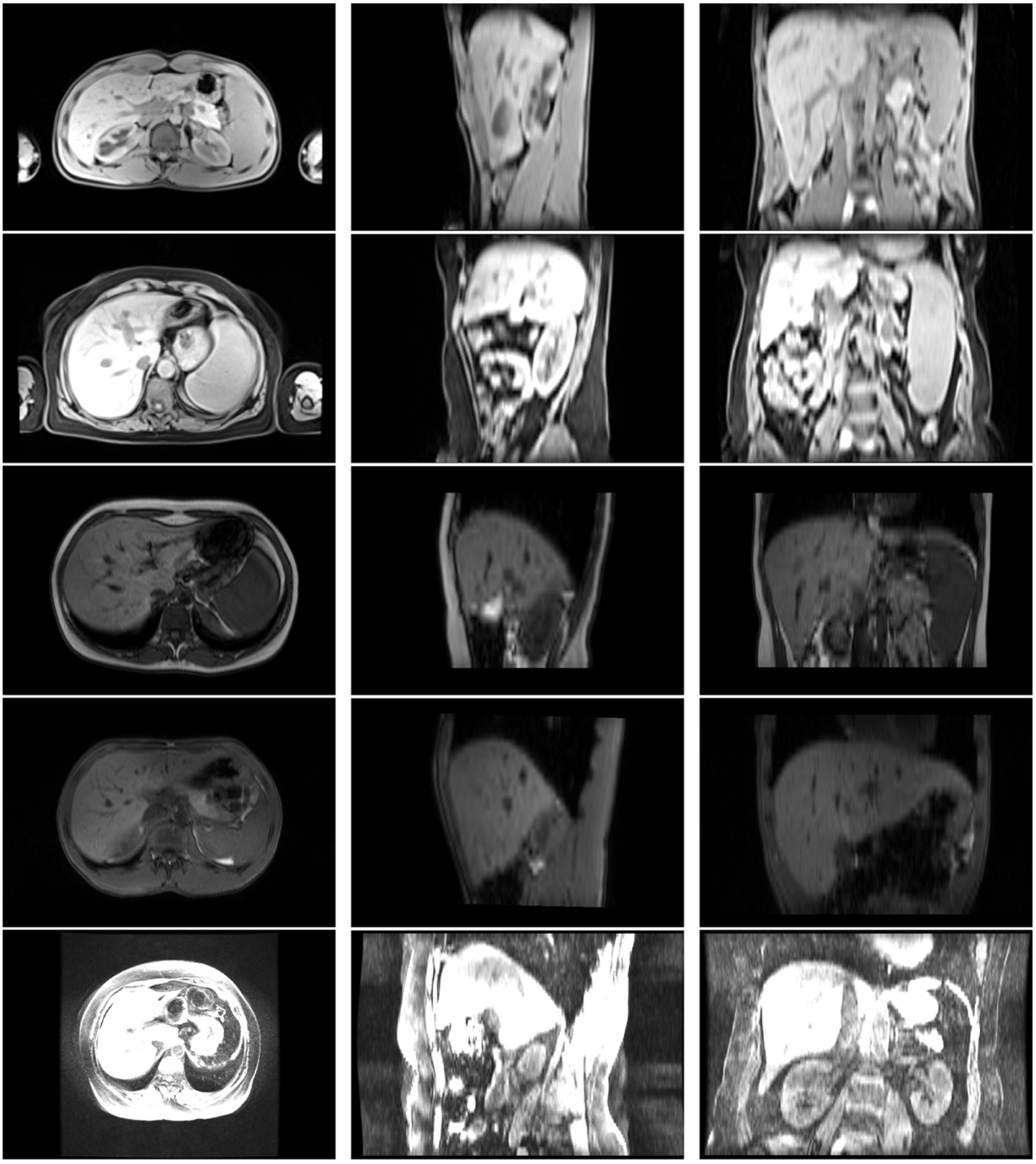

Fig. 2. MR images in a FLD clinical trial. Each row is one subject in axial, sagittal and coronal views.

segmentation method. Rikxoort et al. [37] and Linguraru et al. [43] incorporated atlas-based method into their segmentation framework. However, most generative models are sensitive to data and initialization, while discriminative approaches usually require a large amount of training data with consistent imaging settings, which are label intensive and may not be feasible in clinical trials. Besides, CT images have different appearance patterns with MR images which makes most algorithms designed for CT images not suitable for MRI.

Specifically, there have been some literatures about liver segmentation in MR images. Massoptier et al. [44] initialized graph cut from some preprocessing steps. Platero et al. [45] used level set [16] to segment liver after manual selection of region of interest. Logeswaran et al. [46] proposed a watershed [47] based algorithm to isolate liver in 2D MR images. Siewert et al. [48] proposed an automated method for segmenting liver from contrast-enhanced MRI based on edge detection in 2D slices. Considering the large size and variety of data set in clinical trials, improving the robustness of automatic 3D segmentation is still under research.

Basically, there are two categories of deformable models in the literatures. One is explicit parametric models that use parametric representation for deformable curves or surfaces during the segmentation, such as Snakes or Active Contour Models [13,15]. The other one is implicit geometric models [14,16] that use the level set of a higher-dimensional scalar function to represent curves or surfaces implicitly. Although differ in implementation, both model the segmentation as a energy minimization problem and rely on edge information to derive external forces. Huang et al. [18]

proposed a Metamorphs model which combines the edge and region energy terms to drive the deformable shape.

Some other studies use the deformable models with shape priors are shown promising in cardiac segmentation [20], brain structure segmentation [49] as well as CT liver segmentation [42]. This is because shape constraints can be incorporated to overcome some misleading appearance cues in medical images to make the deformable models more effective. Traditional shape models represent shape distributions by the mean and major variations, for example Active Shape Models (ASM) [50]. These statistical shape models do not handle gross and sparse errors well. In many cases, the initial segmentation is relatively good and deformable model is reliable at most positions, only sparse gross errors instead of Gaussian errors may be observed during the model evolution. Thus, Zhang et al. [51] proposed a sparse shape composite model that can be incorporated into deformable model [52] and get more accurate and effective segmentation result.

A key problem of the deformable models is the reliable initialization. Given a small number of training images and their annotations, learning based object or boundary detectors may not be robust enough in clinical environment. While Slagmolen et al. [53] and Okada et al. [54] demonstrated the atlas-based method can provide a reliable initial segmentation for refinement procedure. Numerous atlas building algorithms have been proposed for human brain [55–57]. Park et al. [58] built a liver probabilistic atlas based on landmarks. Observing the atlas construction is sensitive to the choice and accurate localization of landmarks, Xiong et al. [59] used a landmark-free method based on dense volumes to construct a linear unbiased liver atlas from CT images. Based on these previous studies, we propose a novel framework that combines the atlas-based initialization with shape constrained deformable model to obtain robust liver segmentation in clinical environment.

3. Methodology

In this section, we first introduce our framework for liver segmentation and hepatic fat-fraction assessment. In the second part, the energy terms contributing in the deformable model are discussed in detail. Then we describe the construction of statistical image atlas and shape atlas, and the sparse shape prior representation. At last, some implementation details and the fat-fraction assessment are discussed.

3.1. Algorithm framework

The demonstration of our framework is shown in Fig. 3. As discussed before, our deformable model is initialized from an atlas-based approach. Through atlas construction, we build a statistical image atlas containing one reference intensity image and a corresponding spatial probability map (SPM) image for liver. Meanwhile, one shape atlas for shape representation model is constructed. The SPM and shape model are in the reference image domain. After nonrigidly registering the reference image to target image, we can deform the SPM and shape model to the target image space using the same transformation. Then the deformable model is initialized and evolves to segment the target liver. The deformation is based on the image context information and regulated by learnt shape constraint as well as the initial SPM. Finally, a chemical shift method is applied to assess fat-fraction distribution in the liver which enables the quantitative analysis of fatty liver disease.

The key component of this framework is the robust deformable model. The energy function E is defined as:

$$E = E_{Int} + \kappa_1 E_{Ext} \tag{1}$$

$$E_{Ext} = \int_{\Lambda} P_{Ext}(\mathbf{x}) d\Lambda = \int_{\Lambda} \mathcal{P}_{edge} + \kappa_2 \mathcal{P}_{region} + \kappa_3 \mathcal{P}_{atlas} d\Lambda \tag{2}$$

Here, $\mathbf{x} : \Lambda \subset R^2 \rightarrow R^3$ denotes a surface representing object boundary. κ_1, κ_2 and κ_3 are all scalar parameters used as balances of different energy terms. E_{Int} is the traditional internal energy term constraining shape's tension and rigidity. E_{Ext} is the external energy term, and $P_{Ext} : R^3 \rightarrow R$ is the potential field induced by three parts. $\mathcal{P}_{edge}$ is the image edge potential term which could be defined using gradient magnitude map or edge distance map or GVF. The edge term is used to deform the model towards object boundary. $\mathcal{P}_{region}$ is the interior region based potential [18]. This term provides two-way balloon forces that drive the current model surface towards the predicted object boundary. The predicted ROI boundary is computed from the current model-interior intensity statistics. $\mathcal{P}_{atlas}$ is the potential term to encode the constraints by the spatial probability map which is learnt in atlas construction and nonrigidly transformed to target image space. In addition, the transformed atlas also provides a reliable initialization to the deformable model.

However, several factors often cause ambiguous boundaries which can mislead the energy term encoding. These factors include image noise, intensity inhomogeneity, and similar intensity distributions of nearby organs. In order to deal with such misleading cues, we incorporated a shape prior constraint into our deformable model to get a unified framework. All the energy terms above are designed differentiable with respect to the model parameter (coordinates $\mathbf{x}$). Thus the mesh deformation can be solved as a dynamic system using gradient descent algorithm. In each time step, it is a linear system like standard Finite Element Method (FEM) [60]. To summarize, the segmentation by the evolution of deformable model with shape constraint is described in Algorithm 1. The atlas construction and shape regularization are discussed in Section 3.3. After registering and warping the image atlas to the target domain, we construct the initial surface model by extracting an isosurface from the warped SPM (see Section 3.4 for details). Then the energy terms and force fields are computed for the deformable model before its evolving. Each energy term is described in detail in Section 3.2. To keep up the efficiency of the evolution, the shape regularization is conducted every Dt iterations. The evolution is stopped when the deformation is small enough. At last, the 3D surface model is converted to binary mask image as the segmentation result.

Algorithm 1. Segmentation framework.

Input:
The target image, trained statistical image atlas and shape atlas
Output:
The binary mask of segmented liver in target image
1: compute initial surface model $\mathbf{y}^{(0)}$ based on image atlas registration
2: compute internal and external forces
3: $t = 0$
4: **repeat**
5: $t = t + 1$
6: deform model $\mathbf{y}^{(t-1)}$ to $\mathbf{y}^{(t)}$ using FEM
7: **if** $mod(t, Dt) == 0$ **then**
8: optimize $\mathbf{y}^{(t)}$ using shape constraint to get a new mesh $\mathbf{y}^{(t)}_{\text{refined}}$
9: **end if**
10: **until** deformable model converges
11: convert the surface model $\mathbf{y}^{(t)}$ to mask image

3.2. Energy terms

Now, we discuss all the energy terms contributing in the evolution of the deformable model. They are E_{Int} (Section 3.2.1), $\mathcal{P}_{edge}$, $\mathcal{P}_{region}$ (Section 3.2.2), and $\mathcal{P}_{atlas}$ (Section 3.2.3).

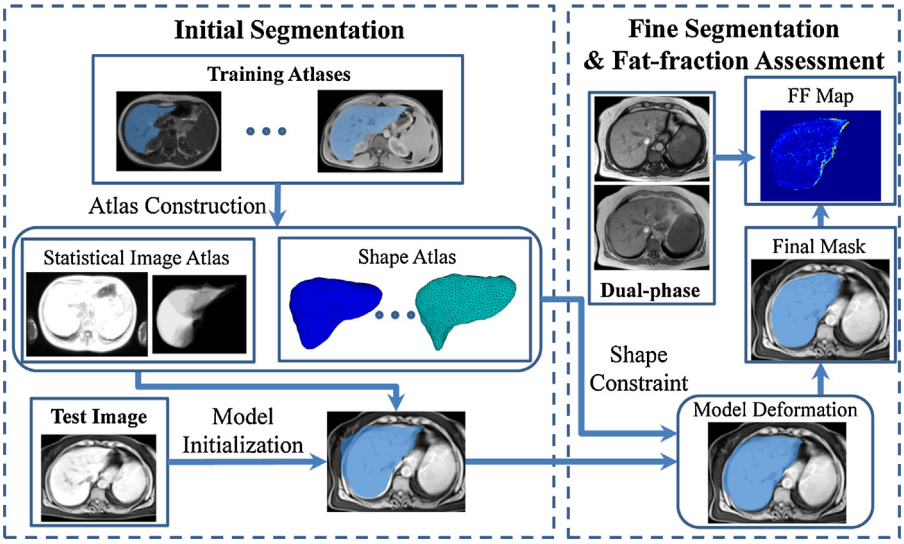

Fig. 3. Segmentation framework.

3.2.1. Internal energy

Let $\mathcal{I} \in R^3$ denote a 3D image. The internal energy E_{Int} which controls the smoothness of deformable model is defined as:

$$E_{Int} = \int_{\Lambda} \{\alpha|\dot{\mathbf{x}}|^2 + \beta|\ddot{\mathbf{x}}|^2\} d\Lambda \tag{3}$$

where $\dot{\mathbf{x}}$ and $\ddot{\mathbf{x}}$ are the first and second derivatives of $\mathbf{x}$ with respect to Λ. $|\dot{\mathbf{x}}|^2$ controls the tension that tends to minimize the surface area. $|\ddot{\mathbf{x}}|^2$ controls rigidity which simulates the surface as a thin plate. α and β are the balancing weights. To solve the minimization problem, the deformable surface must satisfy the Euler–Lagrange equation:

$$\frac{\partial P_{Ext}}{\partial \mathbf{x}} = \alpha\Delta\mathbf{x} - \beta\Delta^2\mathbf{x} \tag{4}$$

where Δ is the Laplace operator. In [61], an umbrella function U is used to approximate the discretization of the differential operators:

$$\Delta(\mathbf{p}) = U(\mathbf{p}) = \frac{1}{n}\sum_i \mathbf{q}_i - \mathbf{p} \tag{5}$$

$$\Delta^2(\mathbf{p}) = U^2(\mathbf{p}) = \frac{1}{n}\sum_i U(\mathbf{q}_i) - U(\mathbf{p}) \tag{6}$$

where $\mathbf{p}$ contains the coordinates of the mesh vertex and $\mathbf{q}_i$ are the neighbors in the triangular mesh we build to represent the surface, while n being the number of neighbors of vertex $\mathbf{p}$. Thus, the right side of Eq. (4) can be re-organized as a matrix, and Eq. (4) is solved by a gradient descent algorithm.

3.2.2. Edge- and region-based energy

The edge potential term is defined in the same fashion as Snakes or GVF. The region potential term is defined similar to the ROI-based balloon term in [18] that allows flexible model initialization:

$$\mathcal{P}_{region}(\mathbf{x}) = \Phi_{\Lambda}(\mathbf{x})\Phi_{ROI}(\mathbf{x}) \tag{7}$$

Here, $\Phi_{\Lambda}(\mathbf{x})$ is the signed distance transform of the current model's surface, $\Phi_{ROI}(\mathbf{x})$ is the signed distance transform of the predicted liver boundary. Given the transformed SPM, both foreground (object) and background statistics are estimated. By applying Bayesian rule, we can compute a binary image representing the most likely object regions. Since the liver is the largest internal organ in the human body, the biggest connected component is the predicted liver region. Here, the region based potential $\mathcal{P}_{region}$ is computed only once before the model evolution based on SPM.

3.2.3. Atlas-based energy

Considering image artifacts, such as unknown noises and bias field, may down-grade the edge- and region-based energy estimations, we introduce the third potential term into the external force to help constraining the deformation field. This potential function comes directly from the transformed SPM:

$$\mathcal{P}_{atlas}(\mathbf{x}) = \Phi_{SPM}(\mathbf{x})^2 \tag{8}$$

where $\Phi_{SPM}(\mathbf{x})$ is a signed distance map to the boundaries of $SPM = \theta$, $\theta \in (0, 1)$. This term keeps the model from shrinking too small to nothing and dilating too big to leak to background. The motivation of such a term is from the observations that the transformed SPM always overlaps nicely with the region of the target liver even the nonrigid registration is not quite accurate. Although the training dataset is relatively small and may not well represent the livers in different pathological populations. The learnt statistical image atlas still contains important spatial probability distribution in abdomen due to the large size of liver.

3.3. Construction of image and shape atlases

In the atlas construction, we build one statistical image atlas and one shape atlas. The statistical image atlas contains one mean intensity image representing a group of training images, and one probabilistic liver map encoding the spatial distribution and variance of liver in the training samples. This statistical image atlas is used as initialization as well as a constraining energy term of the deformable model. The shape atlas is a set of mesh models built from training data which is used to represent the shape prior of liver in the deformable model.

3.3.1. Image atlas

Here we propose a strategy to build the probabilistic liver atlas from MR images similar to [59] by using a state-of-the-art symmetric diffeomorphic normalization (SyN) method [62]. SyN is shown to be one of the top-ranking methods with the best and most consistent accuracy in MRI brain registrations [36]. Let $\omega(\mathcal{I}, \mathcal{D}(\mathbf{x}), \mathcal{J}) \rightarrow \hat{\mathcal{I}}$ denote a nonrigid transformation ω from source image $\mathcal{I}$ to target image $\mathcal{J}$ by deformation field $\mathcal{D}(\mathbf{x})$, and result in a warped image $\hat{\mathcal{I}}$ in the image space of $\mathcal{J}$. Assuming a mapping function

$\phi(\mathbf{x}, t) : \Omega \times t \to \Omega$ parameterizes a family of diffeomorphisms over time t on image domain Ω, and it can be generated by integrating a smooth velocity field $\mathbf{v}$ through the ordinary differential equation:

$$\frac{d\phi(\mathbf{x}, t)}{dt} = \mathbf{v}(\phi(\mathbf{x}, t), t), \phi(\mathbf{x}, 0) = \mathbf{x} \tag{9}$$

where $\mathcal{D}(\mathbf{x}) = \phi(\mathbf{x}, 1) - \mathbf{x}$. Diffeomorphic registration forms the following optimization problem to compute the deformable transformation from moving image $\mathcal{I}$ to fixed image $\mathcal{J}$:

$$\mathbf{v} = \text{argmin}_{\mathbf{v}} \left\{ \int_0^1 \|L\mathbf{v}\|^2 dt + \lambda \int_\Omega \Pi(\mathcal{I}, \phi(\mathbf{x}, 1), \mathcal{J}) d\Omega \right\}. \tag{10}$$

Here, L is an appropriate norm on $\mathbf{v}$, $\Pi(\mathcal{I}, \phi(\mathbf{x}, 1), \mathcal{J})$ is a similarity measurement between $\mathcal{J}$ and warped $\mathcal{I}$ by map $\phi(\mathbf{x}, 1)$. Π could be any similarity metric, and λ controls the degree of exactness in metric-matching. SyN method solves the problem symmetrically to get the deformation field $\mathcal{D}(\mathbf{x})$ and its inverse $\mathcal{D}^{-1}(\mathbf{z})$ at the same time, where $\mathbf{x}$, $\mathbf{z}$ are spatial coordinates in images $\mathcal{I}$ and $\mathcal{J}$.

Given M training simple atlases, our statistical atlas is built following the Algorithm 2. The $\mathcal{I}_i$ and $\mathcal{S}_i$ denote the ith image and its golden standard label image, respectively. As the output, $\overline{\mathcal{I}}$ is the mean image and $\overline{\mathcal{S}}$ is the liver probabilistic map. $\overline{\mathcal{I}}$ is the unbiased representative of the training images. $\overline{\mathcal{S}}(\mathbf{x})$ represents the probability of liver tissue appearing at $\mathbf{x}$. Note that we do not preprocess the training dataset to normalize them into a common size and spacing. Instead, the normalization is implicitly done after the first iteration since all the images are transformed to the normalized template $\overline{\mathcal{I}}^{(0)}$. The result of our atlas construction is shown in Fig. 4.

Algorithm 2. Build statistical atlas.

Input:
The training simple atlases $\{\mathcal{I}_i, \mathcal{S}_i\}, i \in \{1, \ldots, M\}$;
Output:
The statistical atlas $\{\overline{\mathcal{I}}, \overline{\mathcal{S}}\}$;
1: $k = 0$
2: pick an arbitrary m, where $m \in \{1, \ldots, M\}$
3: re-sample $\mathcal{I}_m$ to get isotropic voxel size 1 mm × 1 mm × 1 mm
4: initialize template $\overline{\mathcal{I}}^{(0)}$ by normalized $\mathcal{I}_m$
5: $\mathcal{I}_i^{(0)} = \mathcal{I}_i$, $\mathcal{S}_i^{(0)} = \mathcal{S}_i$
6: **while** $k <$ *MAX_ITERATION* **do**
7: **for** $i = 1$ to M **do**
8: compute the optimal diffeomorphic deformation $\mathcal{D}_i^{(k)}$ to get warped $\mathcal{I}_i^{(k+1)}$ in template space: $\omega(\mathcal{I}_i^{(k)}, \mathcal{D}_i^{(k)}, \overline{\mathcal{I}}^{(k)}) \to \mathcal{I}_i^{(k+1)}$
9: **end for**
10: $\overline{\mathcal{I}}^{(k+1)} = \frac{1}{M} \sum_{i=1}^{M} \mathcal{I}_i^{(k+1)}$
11: $k = k + 1$
12: if converge, break
13: **end while**
14: **for** $i = 1$ to M
15: compute $\mathcal{D}_i^{(k)}$ to get warped $\hat{\mathcal{I}}_i$ and $\hat{\mathcal{S}}_i$: $\omega(\mathcal{I}_i^{(k)}, \mathcal{D}_i^{(k)}, \overline{\mathcal{I}}^{(k)}) \to \hat{\mathcal{I}}_i$, $\omega(\mathcal{S}_i^{(k)}, \mathcal{D}_i^{(k)}, \overline{\mathcal{I}}^{(k)}) \to \hat{\mathcal{S}}_i$
16: **end for**
17: $\overline{\mathcal{I}} = \frac{1}{M} \sum_{i=1}^{M} \hat{\mathcal{I}}_i$
18: $\overline{\mathcal{S}} = \frac{1}{M} \sum_{i=1}^{M} \hat{\mathcal{S}}_i$

During the construction, each nonrigid (deformable) registration is performed after an affine registration. The mutual information (MI) and cross-correlation (CC) are two of the most common image similarity metrics used in registration problems. MI estimates globally optimal matching between images, but may not be a good option in cases where non-stationary patterns require locally adaptive similarity measurement. On the other hand, CC depends only on local estimates and is suitable when locally varying intensities occur. In [63], the authors evaluated different similarity metrics in ANTs [64] toolkit and showed that MI-based affine registration provides the best initialization for deformable registration. They recommended that MI or normalized MI (NMI) as the best similarity metric in dealing with scanner variations and pathomorphological changes. Thus, we use MI metric in affine registration. To ensure the robustness of registration to strong MRI inhomogeneity (bias field), we choose cross-correlation as the similarity metric to do nonrigid registration. In D-dimensional images, it is defined as Eq. (11), where $\mu_{\mathcal{I}_l}$ and $\mu_{\mathcal{J}_l}$ are local means in a n^D-sized window centered at each position $\mathbf{x}$ and $\mathbf{z}$; $\mathcal{I}_l$ and $\mathcal{J}_l$ are vector representations of image patches in the window.

$$CC(\tilde{\mathcal{I}}_l, \tilde{\mathcal{J}}_l) = \frac{(\tilde{\mathcal{I}}_l \cdot \tilde{\mathcal{J}}_l)^2}{(\tilde{\mathcal{I}}_l \cdot \tilde{\mathcal{I}}_l)(\tilde{\mathcal{J}}_l \cdot \tilde{\mathcal{J}}_l)} \tag{11}$$

$$\tilde{\mathcal{I}}_l = \mathcal{I}_l - \mu_{\mathcal{I}_l}, \quad \tilde{\mathcal{J}}_l = \mathcal{J}_l - \mu_{\mathcal{J}_l} \tag{12}$$

3.3.2. Shape atlas

Having the statistical image atlas, a binary template label image can be estimated by thresholding $\overline{\mathcal{S}}$ after smoothing and morphological operations. Then a high-quality surface mesh [65] is built in the template domain. Similarly, all the training label images are converted to high-quality mesh models. To build the shape prior model, we first pre-aligned all the training shapes to the reference shape based on the generalized Procrustes analysis [66] to make sure they are all in the same coordinate space. Then the one-to-one correspondence of vertices on different meshes is obtained by registering the reference mesh to all the training shapes. Here, we employ the mesh quality-preserved deformable models to create the one-to-one correspondence [65]. This method is adapted from the adaptive focus deformable model (AFDM) [67] by registering shapes instead of images.

The sparse shape composite model [51] used to incorporate with deformable model is defined as:

$$\underset{\mathbf{c},\mathbf{e}}{\text{argmin}} \left\| T(\mathbf{y}) - A\mathbf{c} - \mathbf{e} \right\|_2^2 + \lambda_1 \|\mathbf{c}\|_1 + \lambda_2 \|\mathbf{e}\|_1 \tag{13}$$

where $\mathbf{y} \in R^{DN}$ is a vector representing the target shape to be refined, D is the degree of freedom, N is the number of vertexes in the mesh model, $T(\mathbf{y})$ is the transformation (i.e. Procrustes transformation) from target domain to training template domain, $\mathbf{e} \in R^{DN}$ is the sparse error vector, $A \in R^{DN \times M}$ is the matrix of training shapes, $\mathbf{c} \in R^M$ is the sparse coefficient vector. The optimized shape representation is $A\mathbf{c} - \mathbf{e}$, which can be transformed back to input space with the inverse transformation of T.

3.4. Implementation details and fat-fraction assessment

In the construction of statistical image atlas, the nonrigid registration in each iteration requires about $M \times 40$ min. In [59], the authors showed that the convergence for a 15-sized dataset start after 3 iterations. Considering the high cost of computation, we set *MAX_ITERATION* = 3 in Algorithm 2.

The initialization of deformable model is based on one nonrigid registration from atlas mean image to target image. When a unseen target image comes, we compute the deformation field D from $\overline{\mathcal{I}}$ to target $\mathcal{I}_T$. Then target specific liver SPM is estimated by the warped probabilistic map $\omega(D\overline{\mathcal{S}}, \mathcal{I}_T) \to \overline{\mathcal{S}}_T$. An initial liver segmentation $\mathcal{S}_{\text{Init}}$ is computed by thresholding $\mathcal{G}_\sigma * \overline{\mathcal{S}}_T$ with a scalar value θ_T, where $\mathcal{G}_\sigma$ is a Gaussian smoothing filter with scale size σ. This target specific $\mathcal{S}_{\text{Init}}$ is used to build the initial surface mesh for deformable model. And the point correspondence between the target mesh and the reference shape is also computed using the shape registration method in [65].

For the online deformable registration to target image, a simple registration method proposed by [34,68] is used to compute the target registration D_T. This method is based on cubic B-spline interpolation and NMI similarity metric with GPU acceleration. It is much faster than the SyN method at the cost of losing some accuracy. Although the simple registration method produces less

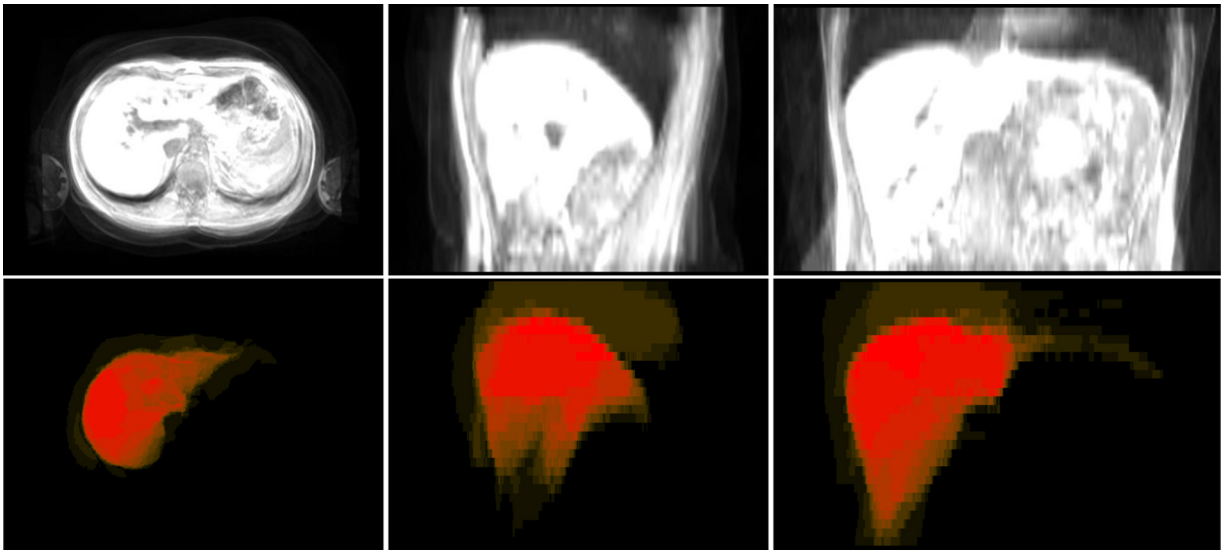

Fig. 4. The mean image and liver probabilistic atlas are shown in axial, sagittal and coronal views. The brightness of red color is proportional to the probability of a voxel belonging to liver tissue. (For interpretation of the references to color in this figure legend, the reader is referred to the web version of this article.)

accurate transformation, the initialization is refined by deformable model afterwards.

The last step of the framework is the hepatic fat measurement. The most commonly used techniques for fat-fraction assessment in MRI is based on a chemical shift approach. Chemical shift approaches can separate the MR signal into fat and water components. They mainly fall in two categories: one uses magnitude data only (magnitude-based) [7]; the other one uses both magnitude and phase information (complex-based) [8,9]. The magnitude-based approach needs two echoes acquired. One at an echo time (TE) in which the water peak and the dominant fat peak are out-of-phase (OP), and one at a TE in which two peaks are in-phase (IP). The two series of images were acquired in a single breath-hold at two sequential TEs. The corresponding TEs are chosen as 2.3/4.6 ms at 1.5 T or 1.15/2.3 ms at 3 T. Based on three assumptions: (1) the fat's signal density is less than the water's signal density ($S_{Fat} \leq S_{Water}$), (2) $S_{OP} = |S_{Water} - S_{Fat}|$ and (3) $S_{IP} = |S_{Water} + S_{Fat}|$, where S_{IP} and S_{OP} denote signal intensities in IP and OP images, the magnitude-based chemical shift method [7] estimates the fat-fraction (FF) map by following equation:

$$S_{Water} = |S_{IP} + S_{OP}|, \tag{14}$$

$$S_{Fat} = |S_{IP} - S_{OP}|, \tag{15}$$

$$FF = \frac{|S_{IP} - S_{OP}|}{2S_{IP}}. \tag{16}$$

The range of fat-fraction is limited to 0–50% due to the absolute value in this method. Therefore, it cannot distinguish fat-dominant or water-dominant tissues. Fortunately, it is acceptable here since fat fractions greater than 50% are uncommon in the liver [9]. Unlike the magnitude-based approach, the complex-based approaches require three of more echoes acquired. Using more information, the complex-based approaches can produce a dynamic range of 0–100% for fat-fraction estimation. But the complex-based chemical shift method is beyond the scope of this work, especially when we do not have prerequisite dataset. In this work, we use the magnitude-based chemical shift method combined with the liver segmentation result to produce liver-specific fat-fraction distributions for quantitative analysis. The experiments in next section demonstrate the robust and accuracy of the proposed methods, and some preliminary results in the hepatic fat assessment.

4. Experiments

In this section, we first describe the dataset and different methods compared in the experiments, as well as the evaluation strategies. Then the detailed results are presented, including visualization of segmentation errors, quantitative and statistical accuracy comparison, and the estimated fat-fraction maps. At last, we discuss about some issues and limitations observed in the experiments.

4.1. Experimental settings

A dataset of abdominal MR volumetric scans for 14 subjects is used for evaluation. This dataset is provided by BioClinica Inc. Each subject has one pair of OP/IP scans taken in a single breath-hold, and one T1-weighted MR scan acquired separately. We choose the T1-weighted MR images to segment liver, whose ground truths were manually labeled by experienced experts. Because the T1-weighted MRI may locate in different coordinate space from that of the corresponding OP/IP scans, we compute a rigid-only registration from T1 MRI to OP or IP MRI and apply the same transformation on the label image. Then hepatic fat-fraction distribution is assessed using IP and OP images with liver mask from T1 MRI data. In the dataset, image resolution ranges from 0.78 to 1.87 mm in the axial slices with slice thickness from 3.5 to 7 mm. The number of slices is from 30 to 104. The range in Z axis varies from 210 mm to 364 mm. The intensity level varies from 178 to 32,767. Some of the samples are shown in Fig. 2.

We compare the proposed method with our implementations of two other methods. One is the atlas based registration method [53] (denoted as ATLAS), and the other one is automatic graph cut method based on probabilistic atlas [69] (denoted as AGC). To make a fair comparison, the atlas construction is the same using the method presented in Section 3.3. The atlas-to-target non-rigid registration is the same. And the graph cut is based on the min-cut/max-flow algorithm [11] assuming 6-neighborhood connectivity. All methods were implemented in Matlab, tested on 3.4 GHz Intel Core i7 computer with 8 G RAM and 1 G-RAM GPU.

The quantitative and statistical comparisons are conducted by leave-one-out cross validation. Each time we choose one sample as the testing and the remaining as the training set. We report the mean value of dice similarity coefficient (DSC), accuracy (ACC)

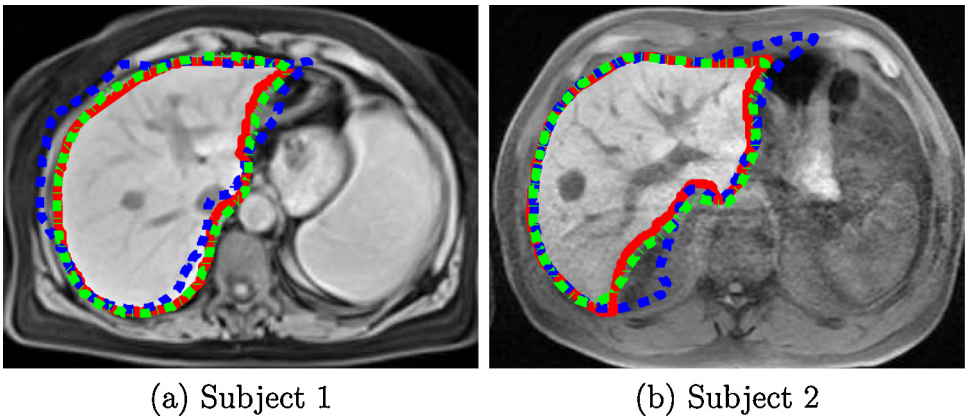

Fig. 5. Visual comparison of initial and final segmentations in an axial slice from two samples. The blue dotted lines are the surfaces of initializations. The green dotted lines are the surfaces of final segmentation results. And ground truth delineations are represented by the red solid lines. (For interpretation of the references to color in this figure legend, the reader is referred to the web version of this article.)

and relative error (RE) compared to the ground truth to show the overlapping accuracy.

$$DSC = \frac{2TP}{2TP + FP + FN}$$

$$ACC = \frac{TP + TN}{TP + TN + FP + FN}$$

$$RE = \frac{FP + FN}{TP + FN}$$

Here, *TP*, *TN*, *FP* and *FN* are number of voxels correctly identified, correctly rejected, incorrectly identified, and incorrectly rejected as liver tissue, respectively. We also measure the symmetrical surface distance error and Hausdorff distance [70] between the surfaces of segmentation results and those of the ground truth. Let X and Y denote point sets of ground truth surface mesh and segmentation result mesh, respectively; $p_X \in X$ is an arbitrary point in X. $\underset{X\to Y}{S}(p_X) = \{p_Y | \|p_X - p_Y\| \le \|p_X - p'_Y\|, \forall p_Y, p'_Y \in Y\}$ represents the point in Y which has the minimum Euclidean distance to p_X. $\underset{Y\to X}{S'}(p_X) = \{p_Y |_{\underset{Y\to X}{S}(p_Y) = p_X}, \forall p_Y \in Y\}$ represents the point set in Y whose closest point in X is p_X. The symmetrical surface distance error at p_X is defined as the maximum Euclidean distance to $\{\underset{X\to Y}{S}(p_X), \underset{Y\to X}{S'}(p_X)\}$. In this way, we can easily measure and compare the surface distance errors referenced to the ground truth.

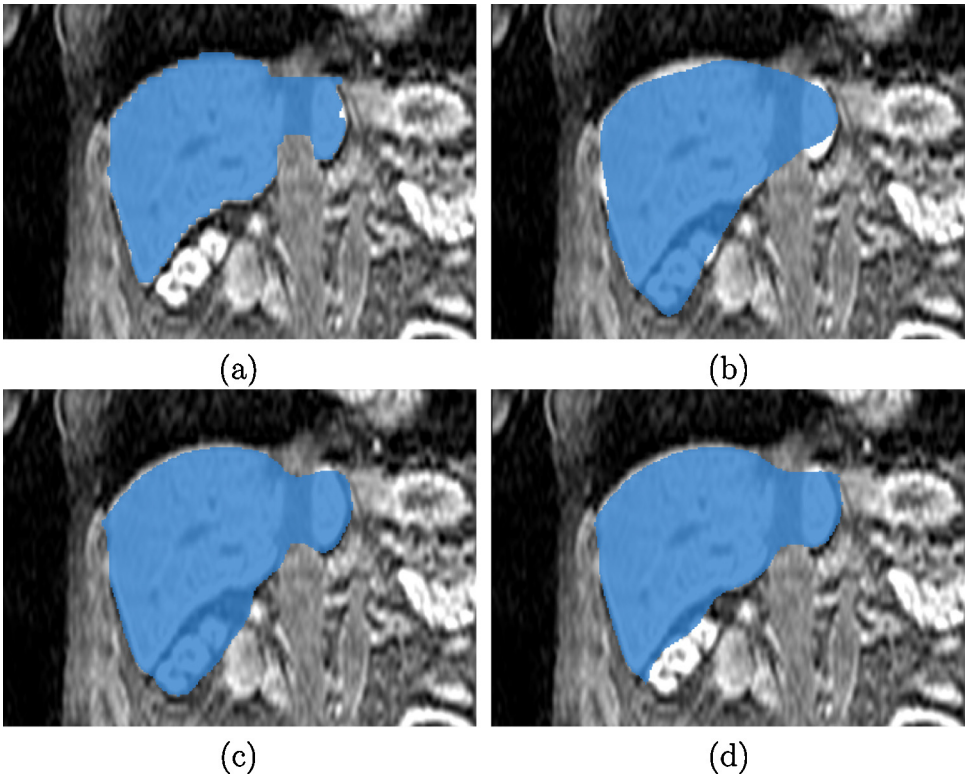

Fig. 6. Visual comparison of proposed deformable model with or without the shape constraint. (a) Ground truth segmentation; (b) the initial segmentation from atlas registration; (c) the result from proposed deformable model without any shape prior; (d) the result from proposed method with the sparse shape prior.

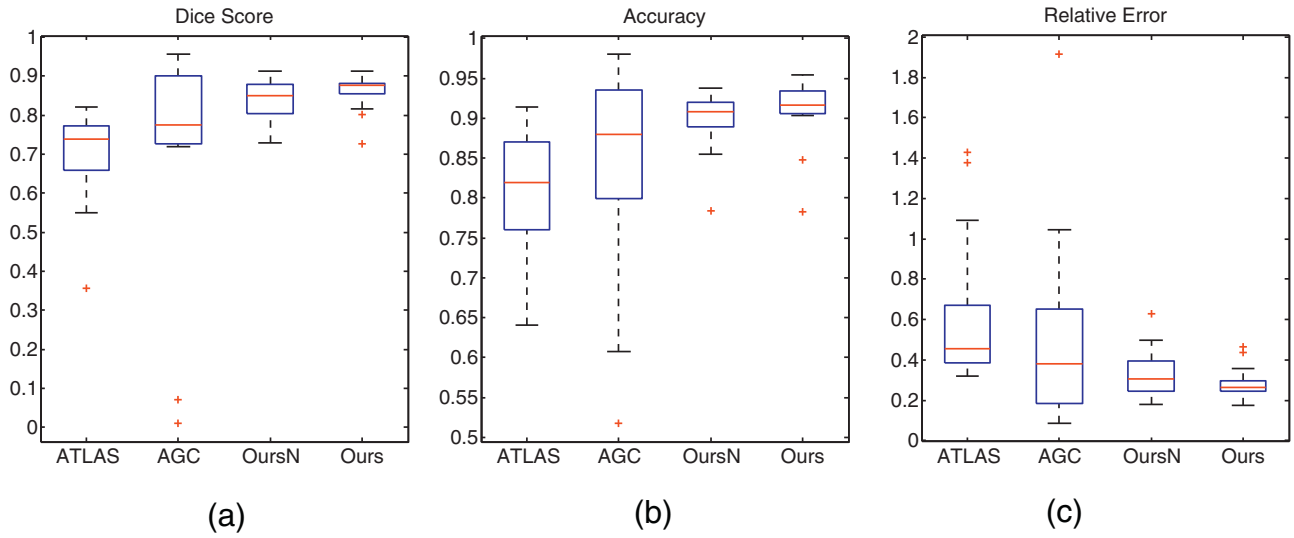

Fig. 7. Statistical comparisons of dice scores (a), accuracies (b) and relative errors (c). In each plot, the four boxes are for ATLAS result, AGC result, OursN result (proposed method without shape constraint), and Ours result (proposed method with shape constraint), respectively.

Let $d(X, Y) = \max_{p_X \in X} \min_{p_Y \in Y} \|p_X - p_Y\|$ denote the forward Hausdorff distance from X to Y. The symmetrical Hausdorff distance is defined as $max[d(X, Y), d(Y, X)]$.

4.2. Results

Before comparing with different approaches, we first show the effect of the deformable model and the shape constraint in our proposed method. As shown in Fig. 5, red lines are ground truth boundaries, blue lines are the initial segmentations, and the green lines are the final results from our proposed approach. We observe that despite its inaccuracy, atlas-based registration provides reliable initialization for the finer segmentation. With the automatic initialization, the deformable model refines the segmentation to fit the real object boundary accurately.

Since the right kidney is very close spatially and has similar intensities to the liver region, the deformable model can easily leak to the kidney region. In Fig. 6, it demonstrates that the sparse shape representation can help to exclude the over-segmented region (i.e. the kidney or heart) effectively.

After showing the effectiveness of our proposed deformable model, we compare the quantitative performances of different approaches. Quantitative comparisons are shown in Table 1. In this table, first row shows the results of ATLAS approach; the second row is from the AGC method; the third row is for the initialization of our method; and the fourth row is for the final results from the proposed method. It shows that our proposed method produce the best performance with respect to the overlapping measurements. It has larger average dice score and accuracy, smaller relative error, as well as smaller variances (σ). The ATLAS approach has relatively small variance but the lowest average performance. The AGC approach is little better than ATLAS in the average performance, but the worst in the variance. Our atlas-based initialization is comparable to ATLAS method, which provides good initialization for our deformable model. The comparison results indicate that the proposed method is accurate and robust comparing with the other

Table 1
Quantitative comparison of segmentations in overlapping measurement. Here, μ is the mean value and σ is the standard deviation of the measurements.

Method	Dice score		Accuracy		Relative error	
	μ	σ	μ	σ	μ	σ
ATLAS	0.70	0.13	0.82	0.07	0.63	0.39
AGC	0.71	0.30	0.84	0.14	0.52	0.49
Initial	0.76	0.13	0.84	0.08	0.58	0.47
Ours	0.86	0.05	0.91	0.05	0.29	0.08

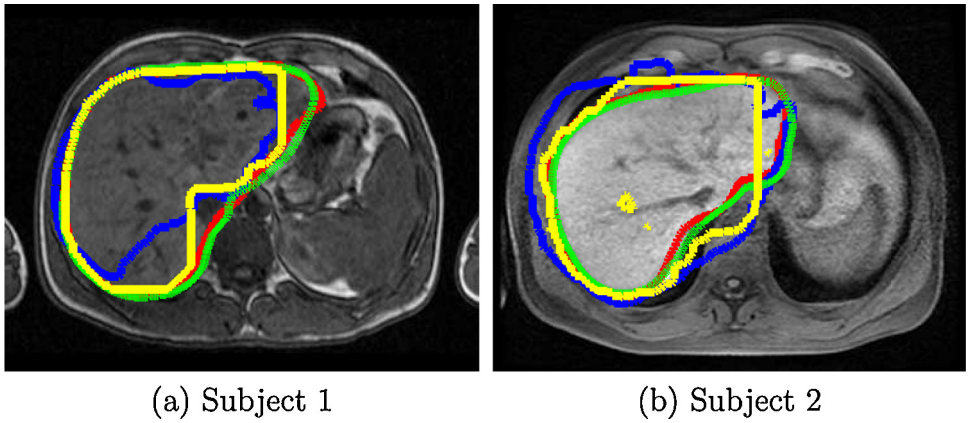

Fig. 8. Visual comparison of ATLAS results (blue lines), AGC results (yellow lines) and our proposed results (green lines) against manual delineations (red lines) in an axial slice from two subjects. (For interpretation of the references to color in this figure legend, the reader is referred to the web version of this article.)

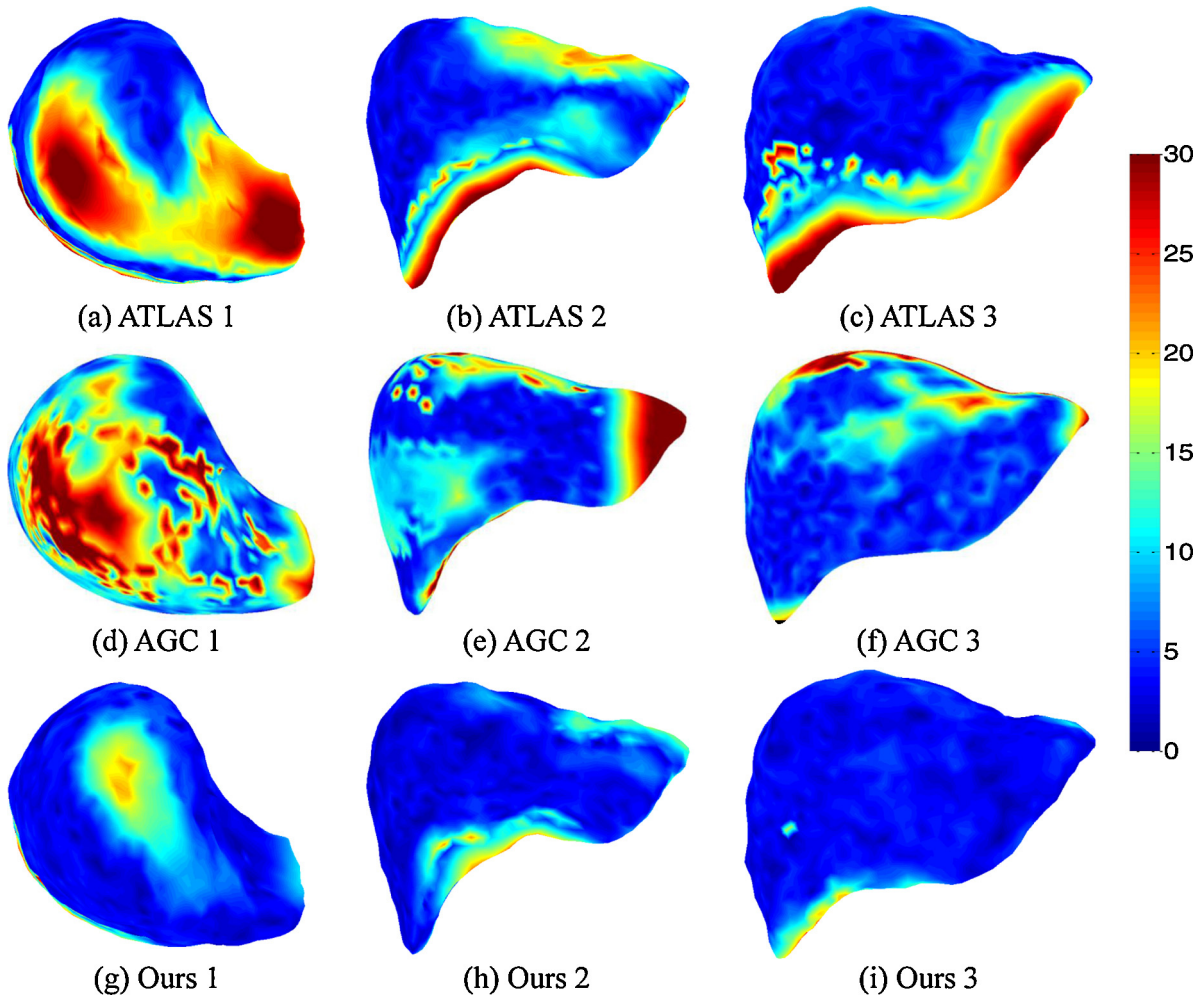

Fig. 9. Visual comparison of surface distance errors for three subjects. Each column is for one subject. First row is for ATLAS segmentations; second row is for AGC results; the third row is for our proposed method.

two approaches. Similar observations are shown in Fig. 7. In this figure, we also plot the proposed method without shape constraint (denoted as OursN) besides the above three methods. Comparing the OursN and Ours method, we observe a slightly better average performance and less variance in the method with shape constraint. As shown in Fig. 6, the difference is not big because the small leaks of deformable model are mainly limited in the nearby kidney or heart regions. Also, the more shape atlas in the training dataset the sparse shape composition should be more accurate to represent the target. Due to the limited training data set in our application, the sparse shape composition may not be beneficial to every testing case.

Fig. 8 compares segmentation results in an axial slice for two subjects. The red lines are ground truth boundaries, blue lines are the segmentations from ATLAS approach, yellow lines are segmentation results by AGC method, and the green lines are the segmentation results from our proposed approach. The ATLAS results are not accurate mainly due to the simple but inaccurate registration we use for the atlas-to-target transformation. The inaccuracy of AGC results may due to the inaccurate initialization and the image inhomogeneities. Fig. 9 shows visual comparisons in 3D view. The surface distance errors are plotted for three subjects (three columns). Fig. 9(a)–(c) shows the surface distances between ground truth and ATLAS method, while Fig. 9(d)–(f) shows the error map for AGC approach. Results by our proposed method are shown in the last row (Fig. 9(g)–(i)), which demonstrate the least errors. The mean surface errors of the segmentations are 17.95 mm, 19.02 mm and 7.07 mm for ATLAS, AGE and Ours method, with standard deviations 16.14, 24.23 and 6.68, respectively. This figure shows that the proposed method has

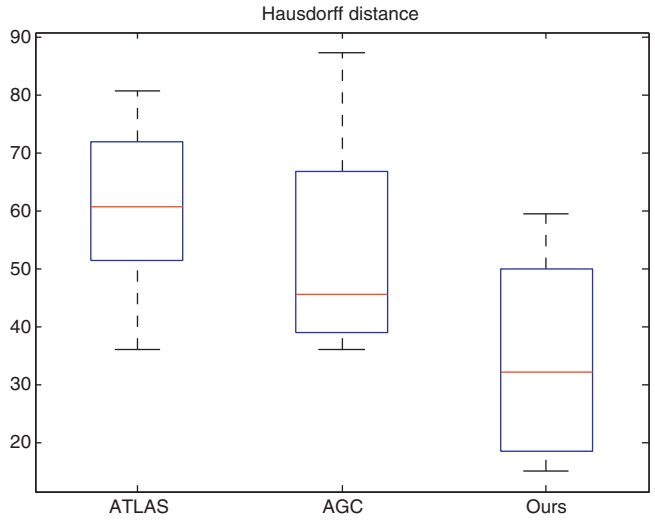

Fig. 10. Statistical comparison of Hausdorff distance for segmentation results by ATLAS, AGC and our proposed method.

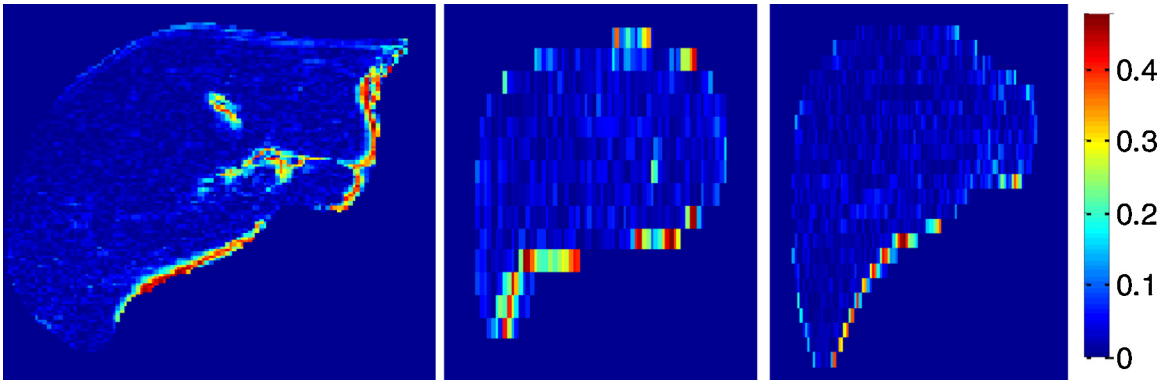

Fig. 11. Colored FFM in liver from different view (axial, sagittal and coronal).Values range from 0% to 50%.

the best performance with regard to the surface distance errors (Fig. 10).

Having shown the performances of the proposed segmentation method, we utilize these segmentation results to compute liver-specific fat-fraction maps using magnitude-based chemical shift method. We transform the segmented liver masks from T1 image domain to the IP/OP image domain by a rigid registration. Then fat-fraction is assessed in the liver region, where each voxel has a scale value indicating the ratio of fat component at that position. With the liver specific FF distribution, it is easy to compute statistical measurements of fat ratio inside the liver tissue automatically. One assessment result is demonstrated in Fig. 11. For this subject, the average fat-fraction inside the liver region is about 0.4%, while the maximum value is about 46% appearing along the liver boundary.

4.3. Discussion

We discuss the running time, parameter sensitivity, implementation issues and limitations here:

(1) For the online segmentation step, most of the time is spent on the nonrigid registration from trained statistical atlas to the testing sample. That is about 4 min per subject. In total, ATLAS method uses about 5 min per subject, AGC method needs about 8 min in total, and the proposed method uses about 8 min. Since AGC is solely based on graph cut algorithm, the cost of memory and time increase dramatically as the image size increases. In our experiments, to ensure isotropic energy measurement, the testing samples are re-sampled to 1 mm × 1 mm × 1 mm resolution. The memory cost for AGC could be up to around 6G bytes in some cases. The memory and time cost are relatively stable in the proposed method, since the deformable mesh model has fixed small number of vertexes independent to image size.
(2) All the parameters used in the methods, including nonrigid registration, deformable model and sparse shape constraint, are tuned experimentally for one case and then apply for all the testing samples. Thus, the above comparison results indicate that our proposed approach has better performance robustly. It will benefit many clinical analyses in the future.
(3) As discussed before, the statistical image atlas is built in three iterations using a limited number of training samples. With such a cheap training step, the proposed deformable model produces robust experimental results. This is an important feature which can benefit in many other segmentation tasks with limited amount of training samples which have large variance.
(4) From our observations, some of segmentation errors from the proposed approach is due to the inaccurate initialization from atlas-to-target registrations, some of the errors is because of the blurred boundaries in low-quality images. In most cases, the errors come from over-segmentations. If the initial segmentation is too big that containing the liver region as well as the entire kidney region inside its boundary, the deformable model can hardly shrink to the correct boundary. This is the main limitation of the proposed framework. In practice, this could be improved by using a more accurate nonrigid registration to align atlas to target sample in the cost of more computation time. And morphologic operations may be an easy and useful way to remove some over-segmentation in a practical view.

5. Conclusion

In this paper we proposed a novel framework to segment 3D liver in MRI, followed by the quantitative assessment of the fat-fraction distribution in the liver region. Specifically, an automatic algorithm is designed to extract liver segmentation robustly for clinical use. This method utilizes symmetric diffeomorphic image registration to learn a statistical image atlas, and uses mesh quality-preserved deformable model to build shape atlases from a limited number of training samples. The statistical image atlas is used to obtain a rough initialization, which is fed into the deformable model for accurate segmentation of liver. Besides the reliable initialization, the statistical atlas also contributes in a region potential energy and a constraining energy for the deformable model. The learnt shape atlases can be used to generate a shape representation model (i.e. sparse shape composition or shape statistics) as a shape prior in the deformable model. Such a robust deformable model enables efficient and accurate liver segmentation, from which the magnitude-based chemical shift method computes the liver specific fat-fraction distribution for quantitative analysis. We extensively validated this method in a clinical dataset of 14 volumetric abdominal MR scans. The results demonstrate that our approach is more robust to various anatomical shapes and diverse data sources coming from different scanners, imaging protocols and scanning parameters, compared to other methods. Since we only used observed feature in T1 weighted MRI, a potential improvement could be more comprehensive boundary features extracted from multi-echo MRIs (i.e. OP/IP images) into the energy term of the deformable model for more accurate segmentation. Besides, the complex-based multi-echo fat assessment algorithm could be investigated if three or more images were acquired. Because the complex-based approach permits a dynamic range of 0–100% for fat-fraction, the proposed framework could become a general solution to fat quantification of other tissues of interest, e.g. adipose, bone marrow, etc. The proposed segmentation framework does not require expensive training or prior knowledge. It is a general framework which can be easily applicable to segmenting other organs, e.g. lung.

Acknowledgments

This project is partially funded by BioClinica Inc. (NSF-MRI-1229628) and Center for Dynamic Data Analytics (NSF I/UCRC, NSFC-61100113).

References

[1] Clark JM, Diehl AM. Nonalcoholic fatty liver disease. J Am Med Assoc 2003;289(22):3000–4.
[2] Sanyal AJ, Campbell-Sargent C, Mirshahi F, Rizzo WB, Contos MJ, Sterling RK, Luketic VA, Shiffman ML, Clore JN, et al. Nonalcoholic steatohepatitis: association of insulin resistance and mitochondrial abnormalities. Gastroenterology 2001;120(5):1183–92.
[3] Angulo P. Nonalcoholic fatty liver disease. N Engl J Med 2002;346(16):1221–31.
[4] Adams LA, Lymp JF, St Sauver J, Sanderson SO, Lindor KD, Feldstein A, Angulo P, et al. The natural history of nonalcoholic fatty liver disease: a population-based cohort study. Gastroenterology 2005;129(1):113–21.
[5] Graif M, Yanuka M, Baraz M, Blank A, Moshkovitz M, Kessler A, Gilat T, Weiss J, Walach E, Amazeen P, et al. Quantitative estimation of attenuation in ultrasound video images: correlation with histology in diffuse liver disease. Invest Radiol 2000;35(5):319–24.
[6] Limanond P, Raman SS, Lassman C, Sayre J, Ghobrial RM, Busuttil RW, Saab S, Lu DS, et al. Macrovesicular hepatic steatosis in living related liver donors: correlation between CT and histologic findings. Radiology 2004;230(1):276–80.
[7] Dixon W. Simple proton spectroscopic imaging. Radiology 1984;153(1):189–94.
[8] Yu H, Shimakawa A, Hines C, McKenzie C, Hamilton G, Sirlin C, Brittain J, Reeder S, et al. Combination of complex-based and magnitude-based multiecho water–fat separation for accurate quantification of fat-fraction. Magn Reson Med 2011;66(1):199–206.
[9] Reeder S, Cruite I, Hamilton G, Sirlin C. Quantitative assessment of liver fat with magnetic resonance imaging and spectroscopy. J Magn Reson Imaging 2011;34(4):729–49.
[10] Pham DL, Xu C, Prince JL. Current methods in medical image segmentation. Annu Rev Biomed Eng 2000;2(1):315–37.
[11] Boykov Y, Funka-Lea G. Graph cuts and efficient ND image segmentation. Int J Comput Vis 2006;70(2):109–31.
[12] Beichel R, Bornik A, Bauer C, Sorantin E. Liver segmentation in contrast enhanced CT data using graph cuts and interactive 3D segmentation refinement methods. Med Phys 2012;39:1361–73.
[13] Kass M, Witkin A, Terzopoulos D. Snakes: active contour models. Int J Comput Vis 1988;1(4):321–31.
[14] Caselles V, Kimmel R, Sapiro G. Geodesic active contours. Int J Comput Vis 1997;22(1):61–79.
[15] Xu C, Prince JL. Snakes, shapes, and gradient vector flow. IEEE Trans Image Process 1998;7(3):359–69.
[16] Chan TF, Vese LA. Active contours without edges. IEEE Trans Image Process 2001;10(2):266–77.
[17] Zhan Y, Shen D. Deformable segmentation of 3-D ultrasound prostate images using statistical texture matching method. IEEE Trans Med Imaging 2006;25(3):256–72.
[18] Huang X, Metaxas DN. Metamorphs: deformable shape and appearance models. IEEE Trans Pattern Anal Mach Intell 2008;30(8):1444–59.
[19] Ling H, Zhou SK, Zheng Y, Georgescu B, Suehling M, Comaniciu D. Hierarchical, learning-based automatic liver segmentation. In: IEEE conference on computer vision and pattern recognition, CVPR 2008. 2008. p. 1–8.
[20] Zheng Y, Barbu A, Georgescu B, Scheuering M, Comaniciu D. Four-chamber heart modeling and automatic segmentation for 3-D cardiac CT volumes using marginal space learning and steerable features. IEEE Trans Med Imaging 2008;27(11):1668–81.
[21] Zhan Y, Dewan M, Zhou XS. Cross modality deformable segmentation using hierarchical clustering and learning. In: Medical Image Computing and Computer-Assisted Intervention – MICCAI 2009. Springer; 2009. p. 1033–41.
[22] Liao S, Gao Y, Shi Y, Yousuf A, Karademir I, Oto A, Shen D, et al. Automatic prostate MR image segmentation with sparse label propagation and domain-specific manifold regularization. In: Information processing in medical imaging. Springer; 2013. p. 511–23.
[23] Guo Y, Zhan Y, Gao Y, Jiang J, Shen D. MR prostate segmentation via distributed discriminative dictionary (DDD) learning. In: ISBI. 2013. p. 868–71.
[24] Van Leemput K, Maes F, Vandermeulen D, Suetens P. Automated model-based tissue classification of MR images of the brain. IEEE Trans Med Imaging 1999;18(10):897–908.
[25] Warfield S, Zou K, Wells W. Simultaneous truth and performance level estimation (STAPLE): an algorithm for the validation of image segmentation. IEEE Trans Med Imaging 2004;23(7):903–21.
[26] Ashburner J, Friston K. Unified segmentation. Neuroimage 2005;26:839–51.
[27] Shi F, Yap P-T, Fan Y, Gilmore JH, Lin W, Shen D. Construction of multi-region-multi-reference atlases for neonatal brain MRI segmentation. Neuroimage 2010;51(2):684–93.
[28] Zhuang X, Rhode KS, Razavi RS, Hawkes DJ, Ourselin S. A registration-based propagation framework for automatic whole heart segmentation of cardiac MRI. IEEE Trans Med Imaging 2010;29:1612–25.
[29] Kim M, Wu G, Li W, Wang L, Son Y-D, Cho Z-H, Shen D, et al. Automatic hippocampus segmentation of 7.0 Tesla MR images by combining multiple atlases and auto-context models. Neuroimage 2013;83:335–45.
[30] Wu G, Wang Q, Zhang D, Nie F, Huang H, Shen D. A generative probability model of joint label fusion for multi-atlas based brain segmentation. Med Image Anal 2014;18(6):881–90.
[31] McInerney T, Terzopoulos D. Deformable models in medical image analysis: a survey. Med Image Anal 1996;1:91–108.
[32] Tsechpenakis G. Deformable model-based medical image segmentation. In: Multi modality state-of-the-art medical image segmentation and registration methodologies. Springer; 2011. p. 33–67.
[33] Shen D, Davatzikos C. Hammer: hierarchical attribute matching mechanism for elastic registration. IEEE Trans Med Imaging 2002;21:1421–39.
[34] Ourselin S, Stefanescu R, Pennec X. Robust registration of multi-modal images: towards real-time clinical applications. In: Medical Image Computing and Computer-Assisted Intervention – MICCAI 2002. Springer; 2002. p. 140–7.
[35] Wu G, Qi F, Shen D. Learning-based deformable registration of MR brain images. IEEE Trans Med Imaging 2006;25(9):1145–57.
[36] Klein A, Andersson J, Ardekani BA, Ashburner J, Avants B, Chiang M-C, Christensen GE, Collins DL, Gee J, Hellier P, et al. Evaluation of 14 nonlinear deformation algorithms applied to human brain MRI registration. Neuroimage 2009;46(3):786–802.
[37] van Rikxoort E, Arzhaeva Y, van Ginneken B. Automatic segmentation of the liver in computed tomography scans with voxel classification and atlas matching. In: MICCAI 2007 workshop proceedings: 3D segmentation in the clinic. Citeseer; 2007. p. 101–8.
[38] Zhang Y, Brady M, Smith S. Segmentation of brain MR images through a hidden Markov random field model and the expectation-maximization algorithm. IEEE Trans Med Imaging 2001;20(1):45–57.
[39] Heimann T, van Ginneken B, Styner M, Arzhaeva Y, Aurich V, et al. Comparison and evaluation of methods for liver segmentation from CT datasets. IEEE Trans Med Imaging 2009;28(8):1251–65.
[40] Gao L, Heath DG, Kuszyk B, Fishman EK. Automatic liver segmentation technique for three dimensional visualization of CT data. Radiology 1996;201:359–64.
[41] Liu F, Zhao B, Kijewski PK, Wang L, Schwartz LH. Liver segmentation for CT images using GVF snake. Med Phys 2005;32:3699–706.
[42] Kainmüller D, Lange T, Lamecker H. Shape constrained automatic segmentation of the liver based on a heuristic intensity model. In: Proceedings of MICCAI workshop 3D segmentation in the clinic: a grand challenge. 2007. p. 109–16.
[43] Linguraru M, Sandberg J, Li Z, Shah F, Summers R. Automated segmentation and quantification of liver and spleen from CT images using normalized probabilistic atlases and enhancement estimation. Med Phys 2010;37:771–83.
[44] Massoptier L, Casciaro S. Fully automatic liver segmentation through graph-cut technique. In: EMBS. IEEE; 2007. p. 5243–6.
[45] Platero C, Poncela J, Gonzalez P, Tobar MC, Sanguino J, Asensio G, Santos E, et al. Liver segmentation for hepatic lesions detection and characterisation. In: ISBI. 2008. p. 13–6.
[46] Logeswaran R, Haw T, Sarker S. Liver isolation in abdominal MRI. J Med Syst 2008;32:259–68.
[47] Haris K, Efstratiadis SN, Maglaveras N, Katsaggelos AK. Hybrid image segmentation using watersheds and fast region merging. IEEE Trans Image Process 1998;7(12):1684–99.
[48] Siewert R, Schnapauff D, Denecke T, Tolxdorff T, Krefting D. Automatic liver segmentation in contrast-enhanced MRI. In: Bildverarbeitung für die Medizin. 2010. p. 405–9.
[49] Shen D, Herskovits EH, Davatzikos C. An adaptive-focus statistical shape model for segmentation and shape modeling of 3-D brain structures. IEEE Trans Med Imaging 2001;20(4):257–70.
[50] Cootes TF, Taylor CJ, Cooper DH, Graham J. Active shape models – their training and application. CVIU 1995;61(1):38–59.
[51] Zhang S, Zhan Y, Dewan M, Huang J, Metaxas DN, Zhou XS. Towards robust and effective shape modeling: sparse shape composition. Med Image Anal 2012;16(1):265–77.
[52] Zhang S, Zhan Y, Metaxas DN. Deformable segmentation via sparse representation and dictionary learning. Med Image Anal 2012;16(7):1385–96.
[53] Slagmolen P, Elen A, Seghers D, Loeckx D, Maes F, Haustermans K. Atlas based liver segmentation using nonrigid registration with a B-spline transformation model. In: Proceedings of MICCAI workshop 3D segmentation in the clinic: a grand challenge. Citeseer; 2007. p. 197–206.
[54] Okada T, Shimada R, Sato Y, Hori M, Yokota K, Nakamoto M, Chen Y-W, Nakamura H, Tamura S, et al. Automated segmentation of the liver from 3D CT images using probabilistic atlas and multi-level statistical shape model. In: Medical Image Computing and Computer-Assisted Intervention – MICCAI 2007. Springer; 2007. p. 86–93.
[55] Evans A, Kamber M, Collins D, MacDonald D. An MRI-based probabilistic atlas of neuroanatomy. In: Magnetic resonance scanning and epilepsy. Springer; 1994. p. 263–74.
[56] Jia H, Wu G, Wang Q, Shen D. Absorb: atlas building by self-organized registration and bundling. Neuroimage 2010;51(3):1057–70.
[57] Shi F, Wang L, Wu G, Zhang Y, Liu M, Gilmore JH, Lin W, Shen D, et al. Atlas construction via dictionary learning and group sparsity. In: Medical Image Computing and Computer-Assisted Intervention – MICCAI 2012. Springer; 2012. p. 247–55.

[58] Park H, Bland PH, Meyer CR. Construction of an abdominal probabilistic atlas and its application in segmentation. IEEE Trans Med Imaging 2003;22(4):483–92.
[59] Xiong W, Ong S, Tian Q, Xu G, Zhou J, Liu J, Venkatash S, et al. Construction of a linear unbiased diffeomorphic probabilistic liver atlas from CT images. In: 16th IEEE international conference on image processing (ICIP). IEEE; 2009. p. 1773–6.
[60] Cohen LD, Cohen I. Finite-element methods for active contour models and balloons for 2-D and 3-D images. IEEE Trans Pattern Anal Mach Intell 1993;15(11):1131–47.
[61] Lürig C, Kobbelt L, Ertl T. Hierarchical solutions for the deformable surface problem in visualization. Graph Models 2000;62(1):2–18.
[62] Avants B, Epstein C, Grossman M, Gee J. Symmetric diffeomorphic image registration with cross-correlation: evaluating automated labeling of elderly and neurodegenerative brain. Med Image Anal 2008;12(1): 26–41.
[63] Avants BB, Tustison NJ, Song G, Cook PA, Klein A, Gee JC. A reproducible evaluation of ants similarity metric performance in brain image registration. Neuroimage 2011;54(3):2033–44.
[64] Avants BB, Tustison N, Song G. Advanced normalization tools (ANTS). Insight J 2009.
[65] Zhang S, Zhan Y, Cui X, Gao M, Huang J, Metaxas D. 3D anatomical shape atlas construction using mesh quality preserved deformable models. Comput Vis Image Understand 2013;117(9):1061–71.
[66] Goodall C. Procrustes methods in the statistical analysis of shape. J R Stat Soc Ser B (Methodol) 1991:285–339.
[67] Shen D, Davatzikos C. An adaptive-focus deformable model using statistical and geometric information. IEEE Trans Pattern Anal Mach Intell 2000;22(8):906–13.
[68] Modat M, Ridgway GR, Taylor ZA, Lehmann M, Barnes J, Hawkes DJ, Fox NC, Ourselin S, et al. Fast free-form deformation using graphics processing units. Comput Methods Programs Biomed 2010;98(3):278–84.
[69] Platero C, Rodrigo V, Tobar MC, Sanguino J, Velasco O, Poncela JM. Probabilistic atlas based segmentation using affine moment descriptors and graph-cuts. In: Computer analysis of images and patterns. Springer; 2011. p. 144–51.
[70] Aspert N, Santa-Cruz D, Ebrahimi T. Mesh: measuring errors between surfaces using the Hausdorff distance. In: Proceedings of IEEE international conference on multimedia and expo, 2002. ICME'02, vol. 1. 2002. p. 705–8.